Mapping of the dark exciton landscape in transition metal dichalcogenides

(article starts on next page)

Mapping of the dark exciton landscape in transition metal dichalcogenides

Gunnar Berghäuser,[1,*] Philipp Steinleitner,[2] Philipp Merkl,[2] Rupert Huber,[2] Andreas Knorr,[3] and Ermin Malic[1]

[1]*Department of Physics, Chalmers University of Technology, SE-412 96 Gothenburg, Sweden*
[2]*Department of Physics, University of Regensburg, 93040 Regensburg, Germany*
[3]*Institut für Theoretische Physik, Technische Universität Berlin, 10623 Berlin, Germany*

Transition metal dichalcogenides (TMDs) exhibit a remarkable exciton physics including bright and optically forbidden dark excitonic states. Here, we show how dark excitons can be experimentally revealed by probing the intraexcitonic $1s$-$2p$ transition. Distinguishing the optical response shortly after the excitation and after the exciton thermalization allows us to reveal the relative position of bright and dark excitons. We find both in theory and experiment a clear blueshift in the optical response demonstrating the transition of bright exciton populations into lower-lying dark excitonic states.

Transition metal dichalcogenides (TMDs) are characterized by tightly Coulomb-bound electron-hole pairs that efficiently couple to light and that can be spin- and valley-selectively excited [1–5]. Recent experimental and theoretical studies show that besides these bright excitonic states, dark optically inaccessible excitons [6–15] play a significant role for the optical response [12,16,17] and the nonequilibrium dynamics in TMDs [13,14,18–20]. In particular, the existence of energetically lower dark exciton states strongly limits the efficiency of light emission in these materials [16,18,21]. We distinguish spin-forbidden dark states, where the Coulomb-bound electron and hole exhibit opposite spin, from momentum-forbidden dark states exhibiting a nonzero center of mass or angular momentum [21]. Both cannot be accessed by light, since photons cannot provide the required spin or momentum to induce an interband transition into these states. Exciton populations occupying dark states can be optically addressed using midinfrared spectroscopy [22,23], however, so far, the focus of these studies has been on revealing the radiative recombination time and the exciton formation dynamics. The exciton landscape and the microscopic origin of different types of dark excitonic states has yet to be addressed. In particular, the spectral position of momentum-forbidden dark excitons has yet to be revealed, leaving the nature of the energetically lowest states unclear.

In this Rapid Communication, we show how the entire excitonic landscape including spin- and momentum-forbidden dark excitons can be identified by investigating the temporal evolution of the intraexcitonic $1s$-$2p$ transition. Our theoretical results, based on a fully quantum-mechanical theory [12,17,24–26], are supported by femtosecond infrared spectroscopy [22,23,27–29] probing intraexcitonic transitions of bright and dark excitons [cf. Figs. 1(a) and 1(b)]. Each excitonic state is characterized by its binding energy, which also determines the $1s$-$2p$ transition energy. As a result, we can identify different excitonic states based on their linear response to an infrared probe pulse. Furthermore, distinguishing the

response shortly after the optical excitation (coherent regime, <100 fs) and after the exciton thermalization (incoherent regime, >1 ps), we can track the exciton dynamics shifting the population from optically excited coherent excitons to incoherent excitonic states that are formed via exciton-phonon scattering [18]. After thermalization, the largest exciton population will be accumulated in the energetically lowest state according to the equilibrium Bose distribution. While the coherent response is always determined by the $1s$-$2p$ transition of the bright exciton with zero center-of-mass momentum $\mathbf{Q}$, the incoherent response will be dominated by the energetically lowest exciton [Figs. 1(b) and 1(c)]. The latter is characterized by a larger excitonic binding energy and thus a higher $1s$-$2p$ separation. As a result, we theoretically predict a clear blueshift in the optical response about 1–2 ps after the optical excitation for materials with dark excitons as the energetically lowest states [Fig. 1(d)]. Our results are supported by femtosecond infrared spectroscopy, where the predicted blueshift for the exemplary material of tungsten diselenide has been demonstrated (Fig. 2).

To map the excitonic landscape in TMDs, we perform calculations on microscopic footing based on the density matrix formalism [30–32] with semiconductor Bloch equations in its core [12,17,25]. To obtain access to the optical response of TMD materials, we first solve the Heisenberg equation of motion for the microscopic polarization $p_{ij}(t) = \langle a_i^\dagger a_j \rangle(t)$ with the creation and annihilation operators $a_i^\dagger$ and a_j and the compound indices i, j containing all electronic quantum numbers, such as the band index λ and the momentum $\mathbf{q}$. The microscopic polarization presents a measure for optical inter- and intraband transitions. To account for the strong exciton physics in TMDs, this microscopic quantity is projected to an excitonic basis with $p_{\mathbf{Q}}^n = \sum_{\mathbf{q}} p_{\mathbf{q},\mathbf{Q}}^{cv} \phi_{\mathbf{q}}^n$ [25,30,31]. The appearing eigenfunctions $\phi_{\mathbf{q}}^n$ are obtained by solving the Wannier equation, which is an eigenvalue equation for the exciton with the index n. Here, we take into account optically accessible bright excitons that are located within the light cone ($\mathbf{Q} \approx \mathbf{0}$). Furthermore, we include momentum-forbidden intervalley dark excitonic states, where the Coulomb-bound hole and electron are located in different valleys. In particular, we include K-$\Lambda^{(\prime)}$ and K-$K^{(\prime)}$
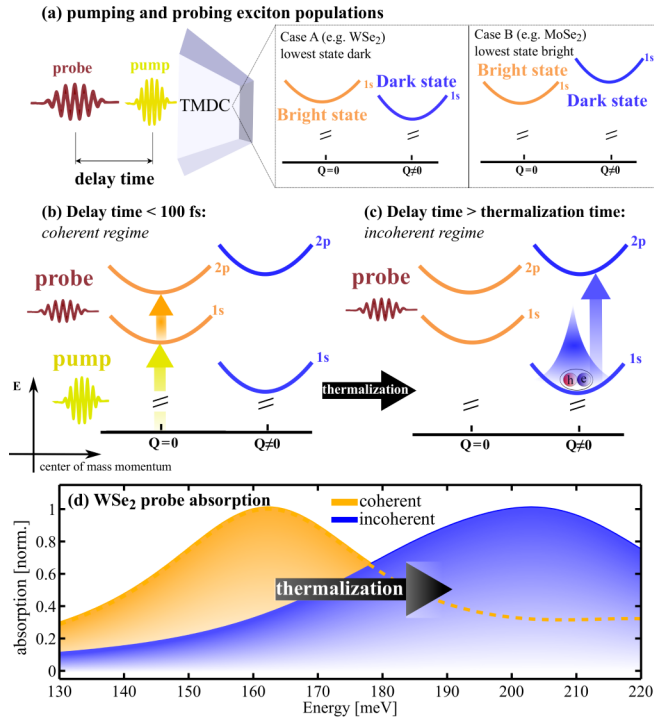
FIG. 1. Theoretically predicted blueshift. (a) Schematic illustration of the modeled experiment, where first, a pump pulse induces a coherent exciton density in the 1s state, which is then probed with a weak pulse matching the energy of the intraexcitonic 1s-2p transition. We can distinguish two scenarios, where the energetically lowest state is either dark or bright. (b) For very short pump-probe delay times (coherent limit), the coherent exciton density has not decayed yet and dominates the linear optical response. (c) For longer delay times, incoherent excitons have already been formed and have thermalized through exciton-phonon coupling. In this incoherent limit, the optical response is dominated by the lowest-lying excitonic states, where the population of incoherent excitons is the largest. (d) Theoretically predicted absorption spectrum for WSe$_2$ in the coherent (yellow area) and incoherent (blue area) regime. The first reflects the population of bright K-K excitons, while the second results from the energetically lowest dark K-Λ excitons.

(Γ-$\Lambda^{(\prime)}$ and Γ-$K^{(\prime)}$) states with the hole at the K (Γ) point and the electron either in the Λ, Λ', K, or K' valley. Here, we also take into account the corresponding spin-forbidden excitonic states, where the Coulomb-bound electron and hole show opposite spin.

The considered many-particle Hamilton operator accounts for the Coulomb interaction, exciton-phonon, and exciton-light interaction. All occurring matrix elements are evaluated within an effective Hamiltonian tight-binding approach and explicitly include TMD characteristic symmetries and coupling strengths. The exciton-phonon interaction has been taken into account to calculate the excitonic linewidths as well as the phonon-assisted formation and thermalization of incoherent excitons [12,18]. The Coulomb interaction is considered within the Keldysh potential [10,25,33–35]. The exciton-light interaction is described by the light-matter Hamilton operator in the $p \cdot A$ gauge [24,36,37] and consists of an intra- and an interband contribution $H_{c\text{-}l} = \sum_\lambda (H_{A \cdot p}^{\lambda \lambda} + H_{A \cdot p}^{\lambda \bar{\lambda}})$. While the

latter is determined by the expectation value of the momentum operator and has been investigated in previous studies [12,25,38], we focus here on the intraband Hamiltonian $H_{A \cdot p}^{\lambda \lambda} = \sum_\lambda j_\lambda(\mathbf{k}) A(t) a_{\lambda \mathbf{k}}^\dagger a_{\lambda \mathbf{k}}$ with $j_\lambda(\mathbf{k})$ as the intraband current projected to the polarization direction $\mathbf{e}_A$ of the incident light field $\mathbf{A}(t) = A(t) \mathbf{e}_A$. The current reads $\mathbf{j}_\lambda(\mathbf{k}) = -\frac{e_0}{\hbar} \frac{\partial \varepsilon_\mathbf{k}^\lambda}{\partial \mathbf{k}} = -\frac{e_0 \hbar}{m_\lambda} \mathbf{k}$ with the effective mass m_λ of the considered band λ [39].

The goal is to calculate the optical response of different monolayer TMDs to a weak infrared probe pulse after coherently pumping the 1s exciton in two limiting cases: (i) In the coherent limit shortly after the pump pulse (delay time $t_{pp} < 100$ fs), when the system is dominated by the optically generated excitonic coherence $p_\mathbf{Q}^n$ [cf. the orange line in Fig. 1(d)]. (ii) In the incoherent limit after exciton thermalization (delay time $t_{pp} > 1$ ps), when all interband coherences have decayed and the optical response is solely determined by the incoherent exciton density $N_\mathbf{Q}^n$ reflecting an equilibrium Bose distribution [cf. the blue line in Fig. 1(d)]. While the pump pulse excites coherent excitons, e.g., creates an excitonic polarization, the infrared probe pulse induces intraexcitonic coherences inducing transitions from 1s to 2p excitonic states [Fig. 1(c)]. To determine the infrared absorption of TMDs, we calculate the macroscopic intraband current, which reads in the excitonic picture,

$$J(t) = \sum_{nm} \sum_\mathbf{Q} j_{nm} \left[p_\mathbf{Q}^{n*}(t) p_\mathbf{Q}^m(t) + N_\mathbf{Q}^{nm}(t) \right]. \qquad (1)$$

This equation contains both the infrared response in the coherent (first term) and incoherent limit (second term). Here, we have introduced the excitonic intraband current $j_{nm} = \sum_{\mathbf{q}, \lambda} j_\lambda(\mathbf{q}) \phi_\mathbf{q}^{n*} \phi_\mathbf{q}^m$ corresponding to the current $j_\lambda(\mathbf{q}) = -\frac{e_0}{m_\lambda} \mathbf{q} \cdot \mathbf{e}_A$ weighted with excitonic wave functions. Here, m_λ denotes the effective mass of the considered electronic band λ. Furthermore, $N_\mathbf{Q}^{nm}$ describes the incoherent exciton density for $n = m$, while in the considered thermalized equilibrium situation the off-diagonal terms $n \neq m$ vanish.

The dynamics of the excitonic polarization $p_\mathbf{Q}^n(t)$ as a response to a weak probe pulse is given by the TMD Bloch equation (cf. Supplemental Material [40]). The exciton distribution $N_\mathbf{Q}^n(t)$ can be obtained by taking into account the phonon-assisted formation of incoherent excitons as well as their thermalization towards an equilibrium distribution. While in a previous work [18] we have performed the full time- and momentum-dependent calculations, here we exploit the obtained thermalized Bose distribution of incoherent excitons. After solving the TMD Bloch equation for the excitonic polarization $p_\mathbf{Q}^n(t)$ in the coherent limit, we have access to the intraband current from Eq. (1). Then, we can determine the optical susceptibility $\chi(\omega) = \frac{J(\omega)}{\varepsilon_0 \omega^2 A_0(\omega)}$, where ε_0 is the vacuum permittivity. Assuming an ultrashort and weak intraband probe pulse and furthermore neglecting terms higher than the fourth order in the field, the linear midinfrared susceptibility reads, in the coherent (χ^c) and incoherent limit (χ^{ic}),

$$\chi^c(\omega) = \frac{1}{\varepsilon_0 \omega^2} \sum_{nm} \left(\frac{|j_{1s,m}| |p_0^n|^2}{\Delta \varepsilon_{m,n} - i \gamma_{0,c}^{mn} - \hbar \omega} \right), \qquad (2)$$

$$\chi^{ic}(\omega) = \frac{1}{\varepsilon_0 \omega^2} \sum_{\mathbf{Q} nm} j_{nm} \frac{\sum_l \left(j_{ml} N_\mathbf{Q}^{nl} - j_{ln} N_\mathbf{Q}^{lm} \right)}{\varepsilon_\mathbf{Q}^m - \varepsilon_\mathbf{Q}^n - i \gamma_{\mathbf{Q}, ic}^{mn} - \hbar \omega}. \qquad (3)$$

Here, we have introduced the quasistatic pump-induced excitonic polarization p_0^n at the time of the probe pulse and a constant dephasing rate for the intraexcitonic transition including $\gamma_{0,c}^{mn} = \gamma_{0,c}^n + \gamma_{0,c}^m$ in the coherent and $\gamma_{Q,ic}^{mn}$ in the incoherent regime. Since a microscopic description of the dephasing rates stemming from higher-order correlations is beyond the scope of this Rapid Communication, we assume a typical constant dephasing of 40 meV [12]. In both regimes, we find that the absorption shows a Lorentzian shape. The spectral position of the Lorentzians is determined by the energy difference of the initial (n) and the final (m) excitonic state. The absorption intensity is given by the optically excited coherent or indirectly formed incoherent exciton populations in the involved states. While the population of the initial state enhances the absorption of the midinfrared probe pulse, the population of the final state leads to negative contributions that could eventually result in gain [41].

Evaluating Eqs. (2) and (3), we can calculate the optical response of TMD materials to an infrared probe pulse both in the coherent regime ($t_{pp} < 100$ fs) directly after the pump pulse and in the incoherent regime after the excitonic thermalization ($t_{pp} > 1$ ps). The corresponding probe absorption is shown in Fig. 1(d) for the exemplary material tungsten diselenide (WSe$_2$). In the coherent limit (yellow area), the initially pumped coherent $1s$ excitons dominate the optical response to the infrared pulse. Here, the pronounced peak is located at 160 meV corresponding to the energy difference between the $1s$ and the $2p$ excitonic state of the bright K-K exciton. Note that the $2p$ exciton consists of the states $2p_+$ and $2p_-$, which are not energetically degenerated due to a nonvanishing geometric phase in TMD monolayers [42]. As a result, we find that the infrared absorption is given by a superposition of two Lorentzian peaks.

For larger delay times between the pump and the probe pulse, incoherent exciton populations are formed [12,18] and have already thermalized into a Bose distribution. Here, predominantly lower energetic states are occupied [cf. Fig. 1(c)]. The excitonic landscape of WSe$_2$ exhibits optically inaccessible dark states well below the initially pumped bright K-K exciton [18]. These momentum-forbidden intervalley excitons (K-Λ) are located at different high-symmetry points of the Brillouin zone. The involved conduction band at the Λ valley shows a significantly larger effective mass compared to the K valley [39], resulting in a higher excitonic binding energy and therefore a larger $1s$-$2p$ separation. In the incoherent regime, we find that the infrared resonance is blueshifted by approximately 40 meV [cf. the blue area in Fig. 1(d)]. The new peak at 200 meV corresponds to the $1s$-$2p$ transition energy of the K-Λ exciton. However, the peak shape deviates from a Lorentzian and is a result of the linear response stemming from multiple dark exciton states. Thus, measuring the $1s$-$2p$ transition allows us to identify different dark exciton states and their relative spectral positions, as will be discussed below.

To test the theoretical prediction, we perform a femtosecond near-infrared pump/midinfrared probe experiment in a WSe$_2$ monolayer. Our samples were prepared by mechanical exfoliation of WSe$_2$ bulk crystals on viscoelastic substrates and were subsequently transferred onto a chemical vapor deposited (CVD) diamond window [43]. All measurements were performed at room temperature and ambient conditions. A 90-fs
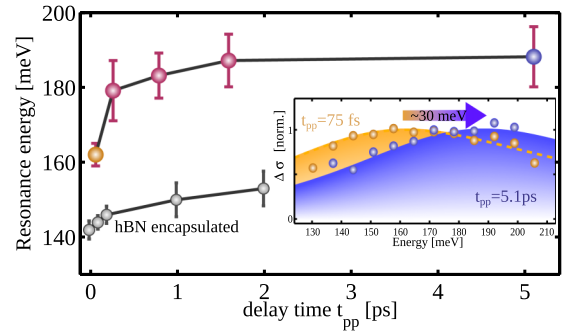

FIG. 2. Experimentally measured blueshift. Resonance energy of the intraexcitonic $1s$-$2p$ transition in a monolayer WSe$_2$ on a diamond substrate as a function of the pump-probe delay time t_{pp} after resonant interband optical injection of coherent A $1s$ excitons. We observe a clear blueshift of roughly 30 meV after a few ps. The error bars represent the 95% confidence interval of the resonance energy. The inset shows the real part of the pump-induced midinfrared conductivity $\Delta\sigma_1$ (corresponding to the optical absorption) as a function of the photon energy for two characteristic pump delay times. Here, colored spheres correspond to experimental data, while shaded areas show the result of the Lorentz-oscillator model [22]. The gray dots in the main figure show another experiment on monolayer WSe$_2$ encapsulated by hexagonal boron nitride (hBN) demonstrating a clear blueshift of the $1s$-$2p$ transition [27].

laser pulse centered at a wavelength of 742 nm selectively injects bright K-K excitons with a vanishing center-of-mass momentum. At a variable delay time t_{pp}, we subsequently probe the $1s$-$2p$ intraexcitonic transition with phase-locked few-cycle midinfrared pulses covering the range of photon energies between 125 and 210 meV. Complete amplitude- and phase-sensitive electro-optic detection of the transmitted probe wave form allows us to extract the real and imaginary part of the dielectric function independently from each other [22] and fit them both with the same set of parameters. This imposes strict limits on the possible values of the fitting parameters. Furthermore, the real part of the dielectric function has a characteristic zero crossing where the optical absorption exhibits its maximum [22]. This makes the extraction of the resonance energy very precise. For the present study, we have applied linearly polarized pump pulses, which optically excite K and K' valleys. Co- and cross-polarized pump and probe measurements are planned for the future and could reveal the different energetic order of p_- and p_+ states.

The inset of Fig. 2 depicts the real part of the pump-induced midinfrared conductivity $\Delta\sigma$ (corresponding to optical absorption) for two characteristic delay times. The pump fluence $\Phi = 16$ μJ/cm^2 is chosen such that a moderate exciton density of approximately 10^{12} cm^{-2} is maintained. Under these conditions, excitation-induced energy renormalization is small and can be neglected (cf. Supplemental Material). For both delay times, a clear peak in $\Delta\sigma$ is observable corresponding to the intraexcitonic $1s$-$2p$ transition [22]. The peak energy of this transition exhibits a distinct blueshift as the delay time increases from 75 fs to 5.1 ps. A more systematic study of the ultrafast evolution of the resonance energy extracted by fitting the experimental data with a Lorentz oscillator is shown in the main panel of Fig. 2. The resonance energy

exhibits a strong blue shift from 162 meV at $t_{pp} = 75$ fs to 179 meV at $t_{pp} = 275$ fs. Within the next few picoseconds the resonance energy still slightly increases, leading to a saturation at a delay time of 5.1 ps and a total blueshift of 26 meV. This observation is in excellent agreement with the theoretical prediction of a blueshift [Fig. 1(d)] during the process of exciton thermalization resulting in a strong occupation of energetically lowest dark excitonic states. Once the thermalization is reached after approximately 2 ps [18], the blueshift is expected to saturate, as observed in the experiment.

Figure 2 also shows experimental results for a WSe$_2$ monolayer covered with hexagonal boron nitride (hBN), where again a clear blueshift due to the transition of bright to dark excitons is observed. The decrease of the initial $1s$-$2p$ transition (from 160 to 140 meV with hBN) can be explained by the enhanced screening [27]. The blueshift of approximately 15–155 meV after exciton thermalization matches the $1s$-$2p$ transition of the stronger bound dark K-K' exciton (cf. Supplemental Material [40]). This implies that the encapsulation with hBN induces significant changes to the exciton landscape. Due to a lattice mismatch of WSe$_2$ and hBN the encapsulation may induce strain and change the orbital configuration in the z direction. Both effects are known to strongly influence the energetic position of the Λ valley [39,44]. However, further studies are needed to fully understand the impact of hBN on the exciton band structure in TMDs.

The excitonic landscape of each TMD material is different and has been controversially discussed in the literature. Although there is a huge number of investigations, e.g., on MoS$_2$, the relative spectral position of dark and bright states is still unclear. While a temperature-dependent photoluminescence (PL) study suggests that the bright excitonic state is the lowest [16], recent experimental data in an in-plane magnetic field imply that there should be a lower-lying spin-forbidden excitonic state [7]. Even theoretical calculations yield different orderings of dark and bright states in different TMD materials [9,19,45,46]. Our approach allows us to directly address this question, since the optical infrared response significantly differs depending on the relative position of bright and dark excitonic states. In Fig. 3, we show a direct comparison of the theoretically calculated infrared absorption of the four most studied TMD materials including (a) WSe$_2$, (b) MoSe$_2$, (c) WS$_2$, and (d) MoS$_2$. Based on DFT-input parameters on the electronic effective masses and band-gap energies [39], we take into account the contribution of bright K-K as well as dark K-$K^{(\prime)}$, K-$\Lambda^{(\prime)}$, and Γ-$K^{(\prime)}$ excitons. A further separation of these states in spin-like and spin-unlike states is discussed in the Supplemental Material [40]. We find that MoSe$_2$ is the only material that does not exhibit a blueshift [cf. Fig. 3(b)]. Surprisingly, we observe a small redshift due to a minor population of spin-unlike K-K and spin-like K-K' excitons [dashed line in Fig. 3(b)]. In contrast, the infrared absorption of all other studied TMDs exhibits pronounced blueshifts in the range of 30–40 meV, suggesting the existence of an energetically lowest dark state.

The dark excitonic landscape of WS$_2$ results in a similar infrared absorption, as already discussed in the case of WSe$_2$, however, exhibiting a larger blueshift and a clearer separation of the contribution of K-K and K-Λ excitons due to the larger effective masses of the Λ valley in WS$_2$ [39]. For MoS$_2$, we
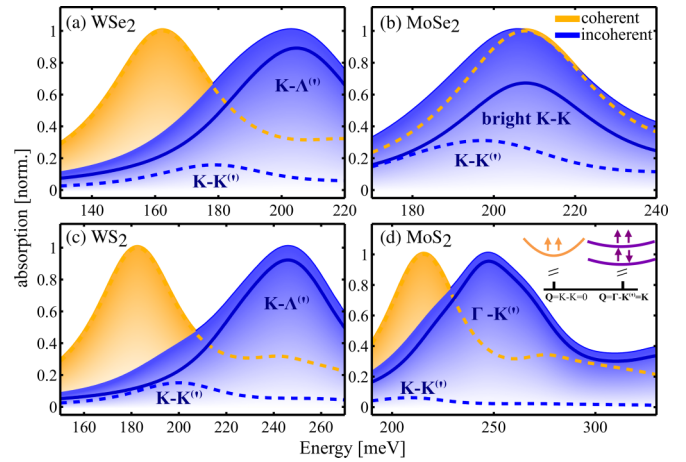

FIG. 3. Comparison of different TMDs. Theoretical prediction of the optical response to an infrared red probe pulse for monolayer (a) WSe2, (b) MoSe$_2$, (c) WS$_2$, and (d) MoS$_2$, distinguishing the coherent (orange) and incoherent (blue) contribution including bright K-$K^{(\prime)}$ as well as dark K-$K^{(\prime)}$, K-$\Lambda^{(\prime)}$, and Γ-$K^{(\prime)}$ excitons. TMDs exhibiting energetically lower-lying dark excitonic states are characterized by a clear blueshift of the incoherent contribution. (a), (c) In W-based TMDs, the equilibrium distribution of excitonic occupation favors the low-lying K-$\Lambda^{(\prime)}$ (solid blue lines) and K-$K^{(\prime)}$ states (dashed lines). (b) In contrast, the major contribution in MoSe$_2$ stems from the bright K-K exciton, revealing that in this material dark states are energetically higher. (d) In MoS$_2$, the lowest states are the dark Γ-$K^{(\prime)}$ excitons. Note that there is no fitting involved in this figure and the spectral position of all excitonic resonances has been microscopically calculated based on the solution of the Wannier equation.

reveal that the major contribution to the infrared absorption stems from the dark Γ-hole excitons, where the holes located at the Γ point have a large effective mass, resulting in a strong excitonic binding energy and consequently a pronounced blueshift of 40 meV of the $1s$-$2p$ transition energy in the incoherent regime. Here, the Coulomb exchange coupling lifts up spin-like states leaving spin-unlike Γ-K excitons as the lowest states (cf. the Supplemental Material [40]). This has already been confirmed in a recent experiment [7], where a brightening of these states has been observed in the presence of an in-plane magnetic field.

In conclusion, we have shown how the excitonic landscape in monolayer transition metal dichalcogenides can be directly mapped by probing the $1s$-$2p$ transition of dark and bright excitons in infrared spectroscopy. We distinguish the optical response shortly after excitation stemming from coherent optically excited excitons and the response after exciton thermalization reflecting the population of energetically lowest incoherent excitons. This allows us to follow the exciton dynamics in different regimes and, in particular, to identify the energetically lowest state. We find that MoS$_2$, WS$_2$, and WSe$_2$ exhibit dark excitons lying below an optically accessible state. Our work sheds light on the fascinating dark excitonic landscape in TMDs and gives insights that will be relevant for the technological exploitation of atomically thin two-dimensional materials.

[1] K. S. Novoselov, A. K. Geim, S. V. Morozov, D. Jiang, M. I. Katsnelson, I. V. Grigorieva, S. V. Dubonos, and A. A. Firsov, Nature (London) **438**, 197 (2005).

[2] K. F. Mak, C. Lee, J. Hone, J. Shan, and T. F. Heinz, Phys. Rev. Lett. **105**, 136805 (2010).

[3] A. Splendiani, L. Sun, Y. Zhang, T. Li, J. Kim, C.-Y. Chim, G. Galli, and F. Wang, Nano Lett. **10**, 1271 (2010).

[4] A. Chernikov, T. C. Berkelbach, H. M. Hill, A. Rigosi, Y. Li, O. B. Aslan, D. R. Reichman, M. S. Hybertsen, and T. F. Heinz, Phys. Rev. Lett. **113**, 076802 (2014).

[5] M. Massicotte, P. Schmidt, F. Vialla, K. G. Schädler, A. Reserbat-Plantey, K. Watanabe, T. Taniguchi, K. J. Tielrooij, and F. H. L. Koppens, Nat. Nanotechnol. **11**, 42 (2016).

[6] Y. Zhou, G. Scuri, D. S. Wild, A. A. High, A. Dibos, L. A. Jauregui, C. Shu, K. De Greve, K. Pistunova, A. Y. Joe, T. Taniguchi, K. Watanabe, P. Kim, M. D. Lukin, and H. Park, Nat. Nanotechnol. **12**, 856 (2017).

[7] M. R. Molas, C. Faugeras, A. O. Slobodeniuk, K. Nogajewski, M. Bartos, D. M. Basko, and M. Potemski, 2D Mater. **4**, 021003 (2017).

[8] X.-X. Zhang, T. Cao, Z. Lu, Y.-C. Lin, F. Zhang, Y. Wang, Z. Li, J. C. Hone, J. A. Robinson, D. Smirnov, S. G. Louie, and T. F. Heinz, Nat. Nanotechnol. **12**, 883 (2017).

[9] F. Wu, F. Qu, and A. H. MacDonald, Phys. Rev. B **91**, 075310 (2015).

[10] T. C. Berkelbach, M. S. Hybertsen, and D. R. Reichman, Phys. Rev. B **92**, 085413 (2015).

[11] H. Dery and Y. Song, Phys. Rev. B **92**, 125431 (2015).

[12] M. Selig, G. Berghäuser, A. Raja, P. Nagler, C. Schüller, T. F. Heinz, T. Korn, A. Chernikov, E. Malic, and A. Knorr, Nat. Commun. **7**, 13279 (2016).

[13] M. Danovich, V. Zólyomi, V. I. Fal'ko, and I. L. Aleiner, 2D Mater. **3**, 035011 (2016).

[14] M. Danovich, V. Zolyomi, and V. I. Fal'ko, Sci. Rep. **7**, 45998 (2017).

[15] C. Robert, T. Amand, F. Cadiz, D. Lagarde, E. Courtade, M. Manca, T. Taniguchi, K. Watanabe, B. Urbaszek, and X. Marie, Phys. Rev. B **96**, 155423 (2017).

[16] X.-X. Zhang, Y. You, S. Y. F. Zhao, and T. F. Heinz, Phys. Rev. Lett. **115**, 257403 (2015).

[17] M. Feierabend, G. Berghäuser, A. Knorr, and E. Malic, Nat. Commun. **8**, 14776 (2017).

[18] M. Selig, G. Berghäuser, M. Richter, R. Bratschitsch, A. Knorr, and E. Malic, 2D Mater. **5**, 035017 (2018).

[19] A. Steinhoff, M. Florian, M. Rösner, G. Schönhoff, T. O. Wehling, and F. Jahnke, Nat. Commun. **8**, 1166 (2017).

[20] A. Steinhoff, M. Rosner, F. Jahnke, T. O. Wehling, and C. Gies, Nano Lett. **14**, 3743 (2014).

[21] E. Malic, M. Selig, M. Feierabend, S. Brem, D. Christiansen, F. Wendler, A. Knorr, and G. Berghäuserm, Phys. Rev. Mater. **2**, 014002 (2018).

[22] C. Poellmann, P. Steinleitner, U. Leierseder, P. Nagler, G. Plechinger, M. Porer, R. Bratschitsch, C. Schuller, T. Korn, and R. Huber, Nat. Mater. **14**, 889 (2015).

[23] P. Steinleitner, P. Merkl, P. Nagler, J. Mornhinweg, C. Schüller, T. Korn, A. Chernikov, and R. Huber, Nano Lett. **17**, 1455 (2017).

[24] R. P. Smith, J. K. Wahlstrand, A. C. Funk, R. P. Mirin, S. T. Cundiff, J. T. Steiner, M. Schafer, M. Kira, and S. W. Koch, Phys. Rev. Lett. **104**, 247401 (2010).

[25] G. Berghäuser and E. Malic, Phys. Rev. B **89**, 125309 (2014).

[26] S. Brem, M. Selig, G. Berghaeuser, and E. Malic, Sci. Rep. **8**, 8238 (2018).

[27] P. Steinleitner, P. Merkl, A. Graf, P. Nagler, K. Watanabe, T. Taniguchi, J. Zipfel, C. Schüller, T. Korn, A. Chernikov, S. Brem, M. Selig, G. Berghäuser, E. Malic, and R. Huber, Nano Lett. **18**, 1402 (2018).

[28] H. J. Joyce, J. L. Boland, C. L. Davies, S. A. Baig, and M. B. Johnston, Semicond. Sci. Technol. **31**, 103003 (2016).

[29] L. Luo, L. Men, Z. Liu, Y. Mudryk, X. Zhao, Y. Yao, J. M. Park, R. Shinar, J. Shinar, K.-M. Ho, I. E. Perakis, J. Vela, and J. Wang, Nat. Commun. **8**, 15565 (2017).

[30] M. Kira and S. W. Koch, Prog. Quantum Electron. **30**, 155 (2006).

[31] H. Haug and S. W. Koch, *Quantum Theory of the Optical and Electronic Properties of Semiconductors*, 5th ed. (World Scientific, Singapore, 2004).

[32] E. Malic and A. Knorr, *Graphene and Carbon Nanotubes: Ultrafast Optics and Relaxation Dynamics*, 1st ed. (Wiley-VCH, Weinheim, 2013).

[33] L. V. Keldysh, JETP Lett. **29**, 658 (1979).

[34] T. C. Berkelbach, M. S. Hybertsen, and D. R. Reichman, Phys. Rev. B **88**, 045318 (2013).

[35] P. Cudazzo, M. Gatti, and A. Rubio, Phys. Rev. B **86**, 075121 (2012).

[36] J. T. Steiner, M. Kira, and S. W. Koch, Phys. Rev. B **77**, 165308 (2008).

[37] S. Leinß, T. Kampfrath, K. V. Volkmann, M. Wolf, J. T. Steiner, M. Kira, S. W. Koch, A. Leitenstorfer, and R. Huber, Phys. Rev. Lett. **101**, 246401 (2008).

[38] G. Moody, C. Kavir Dass, K. Hao, C.-H. Chen, L.-J. Li, A. Singh, K. Tran, G. Clark, X. Xu, G. Berghäuser, E. Malic, A. Knorr, and X. Li, Nat. Commun. **6**, 8315 (2015).

[39] K. Andor, B. Guido, G. Martin, F. Jaroslav, Z. Viktor, D. Neil D, and F. Vladimir, 2D Mater. **2**, 022001 (2015).

[40] See Supplemental Material at http://link.aps.org/supplemental/10.1103/PhysRevB.98.020301 for detailed theoretical description and analyses of excitation induced spectral shifts (see also Ref. [47]).

[41] M. Kira and S. W. Koch, Phys. Rev. Lett. **93**, 076402 (2004).

[42] G. Berghäuser, A. Knorr, and E. Malic, 2D Mater. **4**, 015029 (2017).

[43] A. Castellanos-Gomez, M. Buscema, R. Molenaar, V. Singh, L. Janssen, H. S. J. van der Zant, and G. A. Steele, 2D Mater. **1**, 011002 (2014).

[44] I. Niehues, R. Schmidt, M. Drüppel, P. Marauhn, D. Christiansen, M. Selig, G. Berghäuser, D. Wigger, R. Schneider, L. Braasch, R. Koch, A. Castellanos-Gomez, T. Kuhn, A. Knorr, E. Malic, M. Rohlfing, S. Michaelis de Vasconcellos, and R. Bratschitsch, Nano Lett. **18**, 1751 (2018).

[45] D. Y. Qiu, T. Cao, and S. G. Louie, Phys. Rev. Lett. **115**, 176801 (2015).

[46] J. P. Echeverry, B. Urbaszek, T. Amand, X. Marie, and I. C. Gerber, Phys. Rev. B **93**, 121107 (2016).

[47] A. Chernikov, A. M. van der Zande, H. M. Hill, A. F. Rigosi, A. Velauthapillai, J. Hone, and T. F. Heinz, Phys. Rev. Lett. **115**, 126802 (2015).